scientific reports

Check for updates

OPEN

Surface and in vitro corrosion properties of spark plasma sintered Ti–Zr–Nb–Ta–Ag high entropy alloy for dental implant applications

M. A. Hussein[1,2]✉, A. Madhan Kumar[1,3], N. O. Ogunlakin[1], Nestor Ankah[1] & M. A. Azeem[2]

In this study, the surface and in vitro corrosion behaviors of Ti–Zr–Nb–Ta–Ag high-entropy alloys (HEA) processed through mechanical alloying and spark plasma sintering (SPS) were investigated to assess their potential for dental bioimplant applications. The results showed that the SPS HEA yielded a dual-phase body-centered cubic structure and an ultrafine Zr-based phase. The HEA exhibits nearly double the hardness (8.2 GPa) and significantly higher resistance to plastic deformation (H^3/E^2 =0.0312 GPa) compared to Ti6Al4V, which showed a hardness of 4.11 GPa, and H^3/E^2 value of 0.00349 GPa. X-ray photoelectron spectroscopy revealed the formation of biocompatible surface oxides including TiO_2, ZrO_2, Nb_2O_5, Ta_2O_5 and Ag. The potential of HEA for dental implant applications was evaluated by examining its corrosion behavior in artificial saliva (AS) at different pH values. Compared with Ti6Al4V, the HEA exhibited significantly enhanced corrosion resistance at all pH values. The HEA exhibited the highest charge transfer resistance (1.0805×10^7 Ω·cm²) and the lowest double-layer constant phase element value (0.085 $\mu\Omega^{-1}\cdot cm^{-2}\cdot s^n$), indicating more stable and protective passive film formation. The improved surface characteristics and in vitro corrosion resistance of SPSed HEA demonstrate its potential in dental bioimplants.

Keywords High entropy alloy, Spark plasma sintering, Corrosion, Biomaterials, Dental

Dental implants have become the cornerstone of restorative dentistry, as they offer functional and aesthetic solutions for tooth replacement. The success of these implants depends on key factors including biocompatibility, mechanical strength, and resistance to corrosion in a complex oral environment[1]. Titanium (Ti) and Ti6Al4V alloys are commonly used in biomedical implants owing to their excellent mechanical properties, high strength-to-weight ratio, and corrosion resistance[1]. However, concerns regarding the release of aluminum (Al) and vanadium (V) ions[1], which can cause harmful biological reactions, have led to the pursuit of safer and more advanced alternatives. High-entropy alloys (HEAs) have received considerable attention in recent years owing to their superior mechanical properties, thermal stability, toughness, wear resistance, and corrosion resistance[2,3]. HEAs are composed of multiple principal elements, with nearly equal or unequal atomic ratios. The presence of a high mixing entropy in HEA helps stabilize the solid-solution phase. This high mixing entropy also simplifies the crystal structure of the alloy, eliminating the possibility of a complex intermetallic phase formation[2]. Because of these unique properties, HEAs allow the tailoring of alloy compositions for optimal biological and mechanical performance[3,4]. TiZrNbTaMo HEA was developed for orthopedic implants with a high compressive yield strength ($\sigma y = 1390 \pm 75$ MPa) and plastic strain ($\varepsilon p \approx 6\%$) before failure[5]. The TiZrHfNbTa HEA has been reported to have promising biocompatibility, low modulus, and excellent mechanical characteristics[6]. An equiatomic TiZrNbTa HEA with enhanced mechanical properties was investigated[7]. All the HEA systems mentioned above were synthesized via arc melting. Previous studies[8,9] have indicated that arc melting and its variant, vacuum arc melting (VAM), are frequently used synthetic techniques for HEAs. However, VAM-synthesized HEAs frequently exhibit unfavorable characteristics, including elemental segregation, dendritic microstructures, and coarse grains, which are difficult to regulate. These microstructures frequently exhibit subpar mechanical characteristics, which restricts the use of HEAs in several applications[10]. To address these challenges, powder metallurgy approaches, particularly mechanical alloying (MA) followed by spark plasma

[1]Interdisciplinary Research Center for Advanced Materials, King Fahd University of Petroleum & Minerals, Dhahran 31261, Saudi Arabia. [2]Department of Mechanical Engineering, King Fahd University of Petroleum & Minerals, Dhahran 31261, Saudi Arabia. [3]Department of Aerospace Engineering, King Fahd University of Petroleum and Minerals, Dhahran 31261, Saudi Arabia. ✉email: mahussein@kfupm.edu.sa; mahussein1980@gmail.com

sintering (SPS), have emerged as effective alternatives. MA enables the production of ultrafine-grained, compositionally uniform powders[11] without melting, whereas SPS offers rapid densification with limited grain growth owing to its short processing time. Together, MA and SPS provide superior control over the microstructure and enhance mechanical and electrochemical properties. When alloy elements have a wide range of melting temperatures, casting procedures potentially lack uniformity in the finished alloy[12]. Hence, mechanical alloying, a fully solid-state powder processing technology, can be regarded as a possible alternative method for overcoming the limitations encountered in casting processes. MA is well-known for its simplicity, versatility, economic viability, and scalability for large-scale production. HEAs are typically composed of refractory elements with high melting temperatures, including Ti, Zr, Hf, Nb, Ta, Cr, and Mo[13–15]. The MA approach allows the synthesis of solid solution powders with ultrafine grains and a uniform content[16]. The SPS technology has emerged as a rapid and efficient consolidation technique for metals and amorphous materials. It employs rapid heating and cooling to produce bulk alloy samples with precise control over their microstructure and density. The obvious advantage of SPS is that it reduces grain coarsening owing to the short sintering time[17]. Recent research has highlighted the growing relevance of SPS in biomaterial development beyond that of HEAs. For instance, magnesium-based alloys produced via SPS have shown promising mechanical and physical properties tailored for lightweight and biocompatible applications[18]. Hydroxyapatite has been combined with bioactive glasses (e.g., 45S5) via SPS to produce laminated ceramic composites with improved mechanical integrity[19]. Jayasree et al.[20] fabricated a bi-layered Ti6Al4V–YSZ dental implant using SPS in a single-step process. Similarly, Moayedee et al.[21] employed SPS to develop a functionally graded 3Y-TZP/Ti6Al4V system for dental applications with excellent densification (>99%), high microhardness, and tunable mechanical properties across a gradient. By expanding the material base, Ma et al.[22] produced bioactive Ti–Zn composites using SPS, achieving core–shell microstructures with a balance between strength and elasticity, the SPS technique ensured homogeneous diffusion and microstructure control. Using a different approach, SPS-processed Ti–Mn alloys have been reported to exhibit enhanced mechanical properties[23,24]. Kondo et al.[25] pioneered the use of SPS for fabricating TiN/hydroxyapatite functionally graded material implants that exhibited excellent mechanical strength and osseointegration in vivo. Similarly, Gali et al.[26] used SPS to densify zirconia-reinforced fluormica glass for dental restorations and achieved reduced porosity and enhanced strength, making it suitable for crowns and bridges. Tao et al.[27] reviewed recent developments in TiZr dental alloys and suggested SPS as a potential route for achieving high strength and corrosion resistance in narrow-diameter implants. These studies demonstrate that SPS offers a powerful consolidation strategy for dental implant materials with tailored mechanical, structural, and biological performances. Despite these advances, most SPS-based implant systems still rely on binary or composite systems, with limited studies on HEA specifically tailored for biomaterial and dental bioimplant applications. Razumov et al.[28] investigated high-entropy boride ceramics synthesized using a combined approach of MA and SPS and reported their outstanding material characteristics. Similarly, Naser-Zoshki et al.[29] demonstrated that a non-equiatomic $W_{10}Mo_{27}Cr_{21}Ti_{22}Al_{20}$ HEA processed via MA and SPS formed a BCC solid-solution phase and exhibited excellent compressive strength. These findings underscore the potential of the MA–SPS route to tailor the performance characteristics of HEAs for advanced structural applications. Previous studies have explored how various alloying elements can enhance the biocompatibility and performance of dental materials. Among the various HEAs investigated, the incorporation of biocompatible and corrosion-resistant elements such as zirconium (Zr), niobium (Nb), tantalum (Ta), and silver (Ag) into Ti-based HEAs has garnered particular interest for dental implant applications[30]. Zr improves corrosion resistance and osteoconductivity, thereby supporting bone integration[31]. Studies have shown that adding Zr to Ti alloys promotes better cellular responses[32]. Nb and Ta are valued for their outstanding corrosion resistance and bioinert properties, which limit their ionic release and reduce adverse biological reactions in vivo[33,34]. Ag is commonly incorporated into dental materials owing to its strong antimicrobial properties and enhanced corrosion properties[1]. Despite the growing interest in SPS-processed HEAs, there are no prior reports on the surface and mechanical in vitro corrosion behavior in artificial saliva (AS) of a Ti-Zr-Nb-Ta-Ag HEA developed via MA and SPS for dental implant applications. This study addresses this gap by reporting the surface characteristics and in vitro corrosion performance of artificial saliva of a Ti-Zr-Nb-Ta-Ag HEA fabricated using the MA–SPS route for dental bioimplants. The phase composition and microstructure of the HEA were analyzed using X-ray diffraction (XRD) and field emission-scanning electron microscopy (FE-SEM). The mechanical properties were assessed using microindentation testing. Surface characteristics, including wettability and surface chemistry, were evaluated using contact angle measurements and X-ray photoelectron spectroscopy (XPS). The corrosion properties of the HEA were tested in AS to provide insights into the suitability of the alloy for dental bioimplant applications. The performance of the SPS HEA was compared to that of the commercial Ti6Al4V alloy.

Materials and methods

Material processing

The Ti–Zr–Nb–Ta–Ag (HEA) was processed using a combination of high-energy ball milling and SPS. High-purity elemental powders of Ti, Zr, Nb, Ta, and Ag were weighed to obtain the desired compositions of 35% Ti, 35% Zr, 20% Nb, 5% Ta, and 5% Ag (atomic percentage). The weighed powders were loaded into tungsten carbide (WC) vials with WC balls at a weight ratio of 10:1. To prevent oxidation and contamination, the vials were sealed in high-purity argon atmosphere. The powders were ball milled in a planetary ball mill (Micro Mill PULVERISETTE 7 premium line) at 300 rpm for 20 h. Subsequently, the resulting HEA powder was transferred to a graphite die (20 mm inner diameter) lined with 0.2 mm graphite paper to prevent adhesion during sintering. SPS process was conducted under a controlled vacuum atmosphere, maintaining a vacuum level of approximately 5×10^{-2} mbar using an HPD5 system (FCT GmbH, Germany). During sintering, a uniaxial pressure of 50 MPa was applied and the temperature was increased to 1200 °C for 10 min at a rate of 200 °C/min. To ensure accuracy, the temperature was measured using a thermocouple and a pyrometer. After sintering, the compact was cooled

to room temperature, and the applied pressure was maintained. The final sintered discs obtained from SPS measured approximately 20 mm in diameter and 5 mm in height. Figure 1 shows the schematic of the SPS setup. Several precautions were taken during the mechanical alloying and SPS processes. To reduce oxidation and attrition-related losses, the sealed milling vials were kept in an argon atmosphere of high purity. Furthermore, SPS parameters, such as a short sintering time (10 min) and controlled heating rates, were optimized to reduce volatilization. Post-sintering elemental analyses revealed negligible elemental losses, confirming the integrity of the target alloy composition after processing.

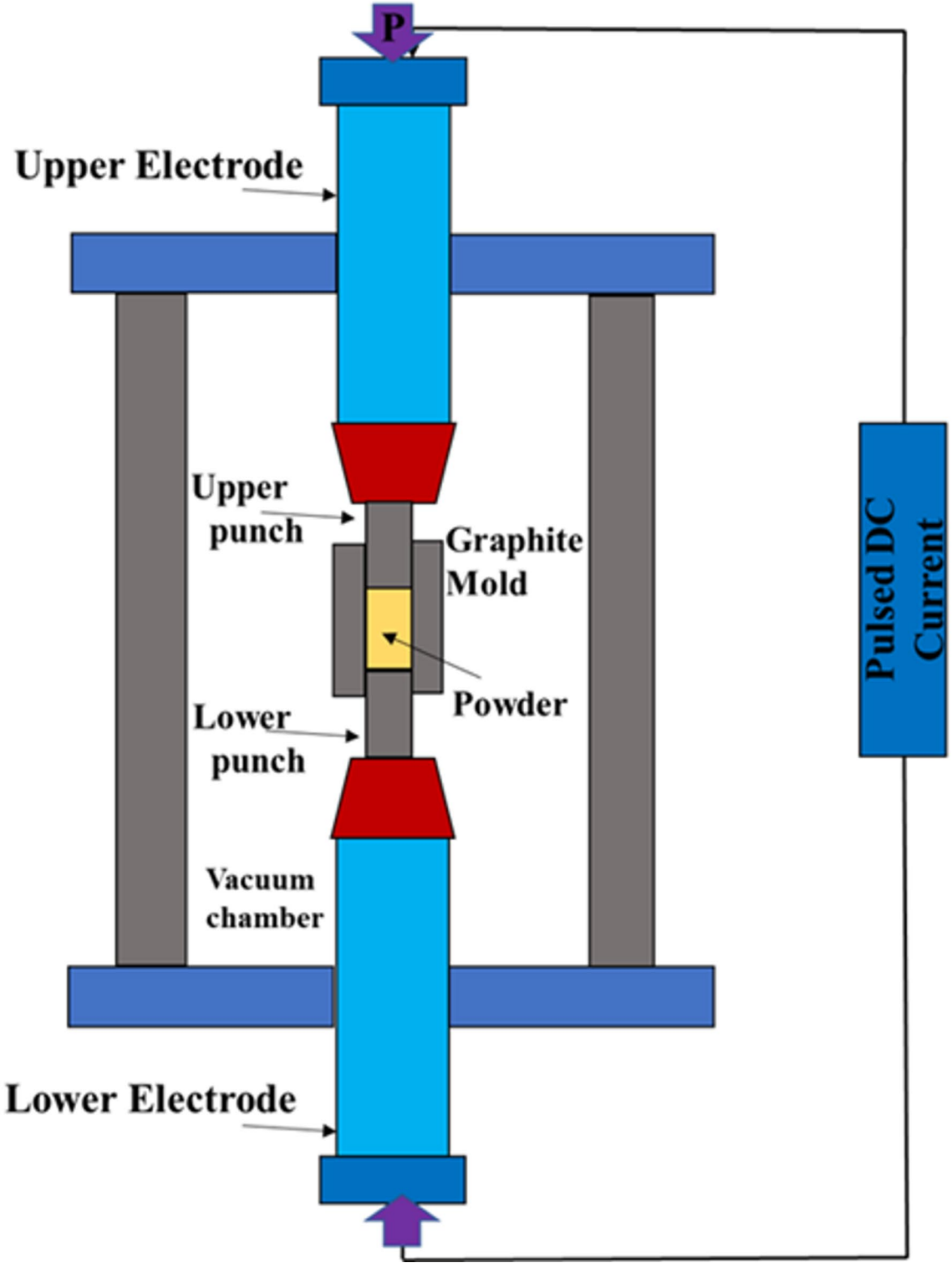

Fig. 1. Schematics of SPS process used for fabrication of Ti–Zr–Nb–Ta–Ag HEA.

Material characterizations

The Ti-Zr-Nb-Ta-Ag HEA was characterized using XRD, FE-SEM, and elemental mapping. X-ray diffraction (XRD) analysis was performed using a diffractometer with Cu Kα radiation at a characteristic wavelength of 0.154 nm. Diffraction patterns were collected over a 2θ range of 20°–90° to identify the crystalline phases present in the alloy. The obtained diffraction peaks were analyzed to determine the phase evolution after mechanical alloying and sintering. For microstructure assessment, samples were prepared using a standard procedure that commenced by employing SiC grinding discs in a series of grit sizes ranging from 240 to 800, followed by fine Al_2O_3 powder to polish the surface until a highly reflective, mirror-like surface was achieved. Subsequently, the samples were etched in a solution containing 5% hydrofluoric acid (HF) and 5% nitric acid (HNO_3) for 3 s to reveal their phases and grain structures. Elemental mapping was performed to visualize the spatial distribution of each constituent element in the HEA.

Micro indentation

The microhardness and modulus of the developed Ti-Zr-Nb-Ta-Ag HEA and the commercial Ti6Al4V alloy were determined using an Anton Paar micro-combi tester with a V-M 53 Vickers indenter with a diamond tip. A controlled force of 100 mN was applied at a loading rate of 200 mN/min, with a 5-second dwell time at the maximum load to ensure uniformity. To obtain representative data, nine indentations were made at 0.5 mm intervals across the sample surface. The Oliver-Pharr method[35] was used to calculate the hardness and modulus values based on the load-unload curves. The contact stiffness, which indicates the resistance of the material to deformation, is calculated using the initial slope of the unloading curve. This method provides detailed insights into the mechanical properties of HEA, allowing for a direct comparison with commercial Ti6Al4V alloys.

Surface analysis of HEA

The surface chemistry, roughness, and wettability of the SPS-ed Ti-Zr-Nb-Ta-Ag HEA were assessed using XPS, a 3D optical profilometer, and contact angle measurements, respectively.

XPS analysis

The surface composition of the oxide layer was analyzed using a Thermo K-Alpha XPS system (Thermo Scientific, Inc.) with a monochromatic Al Kα anode (Kα = 1.486 keV). The measurements were performed using a spot size of 650 µm and an energy step size of 0.1 eV. The surface was subjected to quantitative chemical analysis using the Avantage software to determine the elemental composition and chemical states.

Surface roughness analysis

The surface roughness parameters were evaluated using a 3D optical profilometer (Profilm 3D, Filmetrics, USA) in accordance with the ISO 25,178 standards. To ensure statistical accuracy, arithmetic mean height (Sa), root mean square height (Sq), and maximum height (Sv) were measured at three locations on the sample surface. The Profilm 3D software was used to analyze the data, and the average values were reported to describe the surface topography. Prior to the surface roughness measurements, the samples were ground using silicon carbide paper ranging from 120 to 800 grit size. After grinding, the samples were polished on an emery cloth using a 0.1 µm size Al_2O_3 suspension. Subsequently, they were degreased with acetone and air dried.

Surface wettability analysis

The wetting behavior of the HEA surface was evaluated by measuring contact angles of water and glycerol droplets using a goniometer. Droplets (~ 3 µL) were dispensed from a height of 5 mm to maintain consistent shape and volume. Measurements were performed on polished surfaces to reduce interference from surface roughness. A high-resolution camera equipped with image analysis software was used to capture and analyze the droplet profile, resulting in accurate measurement of contact angles with the HEA surface.

In vitro corrosion behavior in *Artificial saliva* medium

The corrosion behaviors of the SPSed HEA and commercial Ti6Al4V alloy were evaluated in AS using an electrochemical potentiostat (Gamry Reference 3000, USA). Three electrode cell sets were utilized, in which the SPS-HEA samples (exposure area of 1.76 cm^2) acted as the working electrode, whereas a graphite rod and saturated Ag/AgCl electrode were used as the counter and reference electrodes, respectively. AS (Fusayama–Meyer type) contained 0.400 g/L NaCl, 0.400 g/L KCl, 0.795 g/L $CaCl_2{\cdot}2H_2O$, 0.690 g/L $NaH_2PO_3{\cdot}2H_2O$, 0.005 g/L $Na_2S{\cdot}9\ H_2O$, and 1.000 g/L urea, with the pH adjusted to approximately 6.75–7.00. Corrosion tests were performed using AS solutions with pH values of 3.0, 4.9, and 6.8, representing possible intraoral environments[36]. Before each set of corrosion measurements was conducted, the open-circuit potential (OCP) was observed for approximately 1800 s to ensure that the system under investigation attained steady-state conditions. Electrochemical impedance spectroscopy (EIS) tests were performed in the frequency range of 1 kHz to 1 mHz. Electrochemical frequency modulation (EFM) tests were performed by applying an amplitude of 10 mV to the potential perturbation signal and selecting two sine waves (at frequencies of 2 and 5 Hz). Further, potentiodynamic polarization (PDP) experiments were conducted over a potential range from + 250 mV versus OCP to − 2000 mV versus Ag/AgCl at a sweep rate of 1 mV s^{-1}. All corrosion tests were conducted at least three times to verify reproducibility.

Results and discussion

Structure and microstructure analysis

After mechanical alloying for 20 h, the XRD pattern (Fig. 2-a) reveals the formation of a single-phase solid-solution BCC phase indexed with crystallographic planes of (110), (200), (211), and (220). The decrease in peak intensity

and increase in FWHM after MA, as compared to the blended HEA Powders, indicate a reduced crystallite size[37]. The XRD analysis of the Ti-Zr-Nb-Ta-Ag HEA after 20 h of MA followed by SPS, as depicted in Fig. 2-b, provides important insights into the phase evolution and crystallinity of the HEA. Initially, the mechanical alloying process of HEA resulted in a single-phase body-centered cubic (BCC) structure, indicating that the constituent elements (Ti, Zr, Nb, Ta, and Ag) were successfully homogenized into a solid solution. However, the subsequent SPS process resulted in the formation of two distinct BCC phases, BCC1 and BCC2, as well as a Zr-based phase. The XRD pattern of the as-blended HEA powder before ball milling revealed a crystallite size of 27.59 nm and a calculated lattice strain of 0.32%. The low lattice strain indicates that the as-blended powder had a stable and relaxed crystal structure with little internal stress or defects. Mechanical alloying via ball milling considerably affects the crystallite structure and strain of the HEA powder. Ball milling induces severe plastic deformation and introduces significant dislocation densities, resulting in a dramatic reduction in the crystallite size to 3.78 nm and an increase in the lattice strain to 1.98%. This is consistent with the grain refinement and strain-hardening mechanisms typically associated with high-energy milling processes[38]. The increased strain is a direct result of the mechanical alloying process, which introduces many flaws and dislocations into the material. Subsequently, spark plasma sintering of HEA led to additional microstructural changes that resulted in partial recovery and recrystallization. The XRD pattern of the SPS-treated sample revealed two BCC phases, BCC1 and BCC2, and a Zr-containing phase. The crystallite size increased to 21.7 nm for the BCC1 phase, 15.8 nm for the BCC2 phase and 23 nm for the Zr-containing phase indicating a significant coarsening relative to the ball-milled powder while still significantly finer than the as-blended powder. This increase in crystallite size was due to the thermal energy delivered by SPS, which stimulated the grain growth and recrystallization. The reduced lattice strain of 0.546% in the SPS-ed material suggests a partial relaxation of the residual stresses introduced during ball milling, which is facilitated by the thermal and pressure conditions inherent in SPS. The formation of a Zr-based phase alongside the BCC1 and BCC2 phases indicated partial Zr segregation during the sintering process. The larger atomic size of Zr, which possesses three to four orders of magnitude greater mobility than Ta,

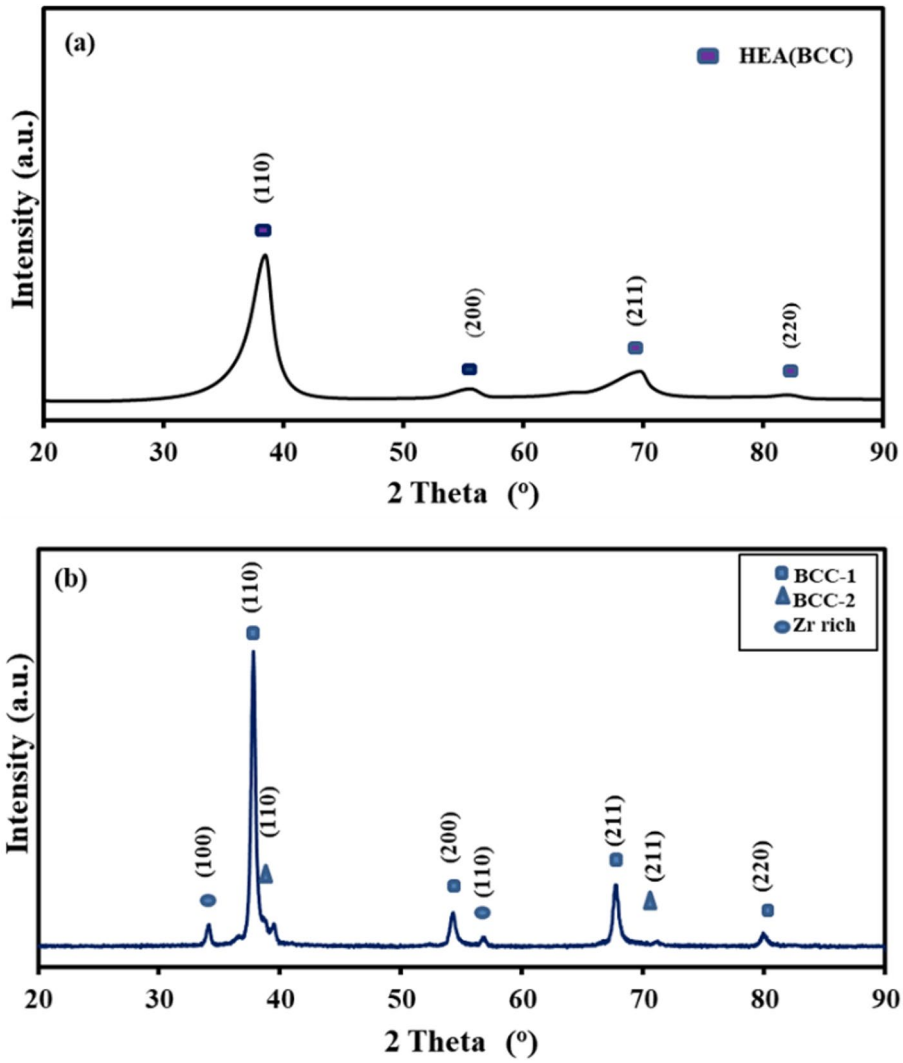

Fig. 2. XRD pattern of mechanically alloyed and SPS HEA: (**a**) MA, (**b**) SPSed HEA.

Nb, and Ti, explains this segregation[39]. The morphologies of the as-received blended powders and ball-milled HEA powders have been previously explained[40]. The microstructural analysis of the SPSed-HEA using FE-SEM is shown in Fig. 3. Post-SPS, the HEA exhibited a microstructure dominated by a primary BCC1 phase grain, a BCC2 minor phase, and a minor Zr-rich phase grain boundary. The observed minor Zr-rich phase segregations, primarily located at the grain boundaries, are attributed to the larger atomic radius and higher diffusion rate of Zr relative to other elements. It is essential to emphasize that these segregations are uniformly distributed and integrated within the alloy matrix rather than forming isolated particles, thus maintaining overall alloy homogeneity. The microstructure of the SPS-ed HEA consisted of a fine-grained composition that included two BCC phases, labeled BCC1 and BCC2, along with a Zr-rich phase (Fig. 3b). Furthermore, the EDS mapping of HEA elements, as depicted in Fig. 3c, indicated minimal segregation of elements and a uniform microstructure as a result of MA and the subsequent SPS process. The line EDS spectrum also confirmed the Zr-rich phase in the microstructure of the SPS-treated HEA, as shown by the sharp Zr peak in the equiaxed dark phase represented in the microstructure. Both the mapped and line EDS results confirm the composition of the elements used in the development of the SPS-treated HEA samples. The transformation from a single BCC phase formed after MA to dual BCC and Zr-rich phases in the SPS-HEA may be ascribed to various factors. Mechanical alloying produces a high concentration of defects and dislocations in the material, which serve as nucleation sites for new phases and promote the formation of multiple phases. Moreover, mechanical alloying facilitates atomic diffusion by augmenting particle contact and minimizing diffusion distances, thereby enabling the segregation of various elements and the development of distinct phases. Phase separation has been documented to obstruct the development of a singular BCC solid solution phase[41]. The higher energy input and enhanced diffusion rates can surpass high-entropy stabilization, leading to the emergence of multiple phases. Consequently, empirical observations suggest that the high-entropy effect does not consistently provide robust stabilization for a singular solid-solution phase. The details of the phase separation phenomenon and thermodynamic calculations have been discussed and explained elsewhere[30,40].

Micro indentation

The results of the ambient-temperature microindentation tests on the SPS-ed HEA sample and commercially available Ti6Al4V sample are presented in Table 1, and the corresponding loading and unloading curves are presented in Fig. 4. The SPS-ed HEA sample exhibited a significant improvement in hardness compared to that of the commercial Ti6Al4V alloy. The hardness of the SPS-ed HEA was nearly twice that of Ti6Al4V and higher than that of the same HEA processed using the conventional sintering technique[30] (Table 1). The improved hardness of the SPS-HEA can be attributed to its refined microstructure, multicomponent alloying effects, and presence of multiple phases. The significantly smaller crystallite sizes and higher lattice distortion resulting from severe plastic deformation during ball milling coupled with controlled recrystallization during SPS led to an enhanced resistance to dislocation motion. Additionally, the synergistic strengthening effects of elements such as Nb, Ta, and Zr, combined with the unique phase interactions, contribute to the superior mechanical properties. These factors collectively enable the SPS-ed HEA to achieve a higher hardness, making it a promising candidate for dental applications in which implants are subjected to wear, deformation, and surface damage due to repetitive chewing and other mechanical actions. The superior hardness of HEAs enhances their wear resistance and durability, thereby contributing to implant longevity and minimal risk of surface damage during extended usage. These properties are critical in high-stress regions of the oral cavity, where traditional materials may fail owing to wear-induced deterioration[42]. The elastic modulus of the SPS-ed HEA was slightly higher than that of Ti6Al4V. Although materials with lower elastic moduli are generally preferred to reduce stress shielding[30], the use of high-modulus materials in dental implants, such as Ti6Al4V (~ 110–140 GPa), can still be justified based on several factors. These materials offer high mechanical strength and corrosion resistance, which are essential for long-term durability and structural integrity of dental implants under high occlusal loading conditions. The high modulus ensures minimal elastic deformation, which maintains implant stability and prevents micromotion at the bone–implant interface, a critical requirement during the early stages of osseointegration[43]. While efforts are ongoing to develop low-modulus β-type titanium alloys to address stress shielding[44], conventional high-modulus materials continue to be accepted owing to their proven reliability and biocompatibility. Another critical factor is resistance to plastic deformation, as indicated by the H^3/E^2 ratio[45]. For SPS-ed HEA, this ratio was calculated as 0.0312 GPa, which is significantly higher than that of 0.00349 GPa for Ti6Al4V. This higher ratio reflects a higher resistance to plastic deformation, further enhancing the wear resistance of HEAs compared to that of traditional titanium alloys. Wear resistance is especially critical for dental implants as it directly correlates with reduced material degradation and enhanced implant performance over time[46]. The superior mechanical properties of the SPS-ed HEA can be attributed to its refined microstructure and the presence of multiple strengthening mechanisms, including solid-solution strengthening and grain boundary strengthening, resulting from its multicomponent composition and optimized SPS conditions. The advanced SPS processing method promotes grain refinement and increases material density, significantly reducing porosity while enhancing the hardness and mechanical performance[47]. The high density and fine microstructure of HEAs provide additional benefits in reducing fatigue failure, which is a common concern for dental implants that are usually subjected to cyclic loading and abrasive forces. Ti6Al4V, which is extensively used in biomedical applications, has raised concerns owing to the presence of alloying elements. Al has been implicated in neurological disorders and V toxicity has also been documented, raising the potential risk of adverse biological reactions[48]. In contrast, the HEA composition (Ti-Zr-Nb-Ta-Ag) consists of elements known for their biocompatibility[30,40,49]. These elements are biocompatible and have no toxic effects, making them particularly suitable for biomedical applications including dental implants. Furthermore, the inclusion of Ag in HEAs enhances their antibacterial properties, a critical factor in preventing peri-implant infections, which are a leading cause of implant failure[50].

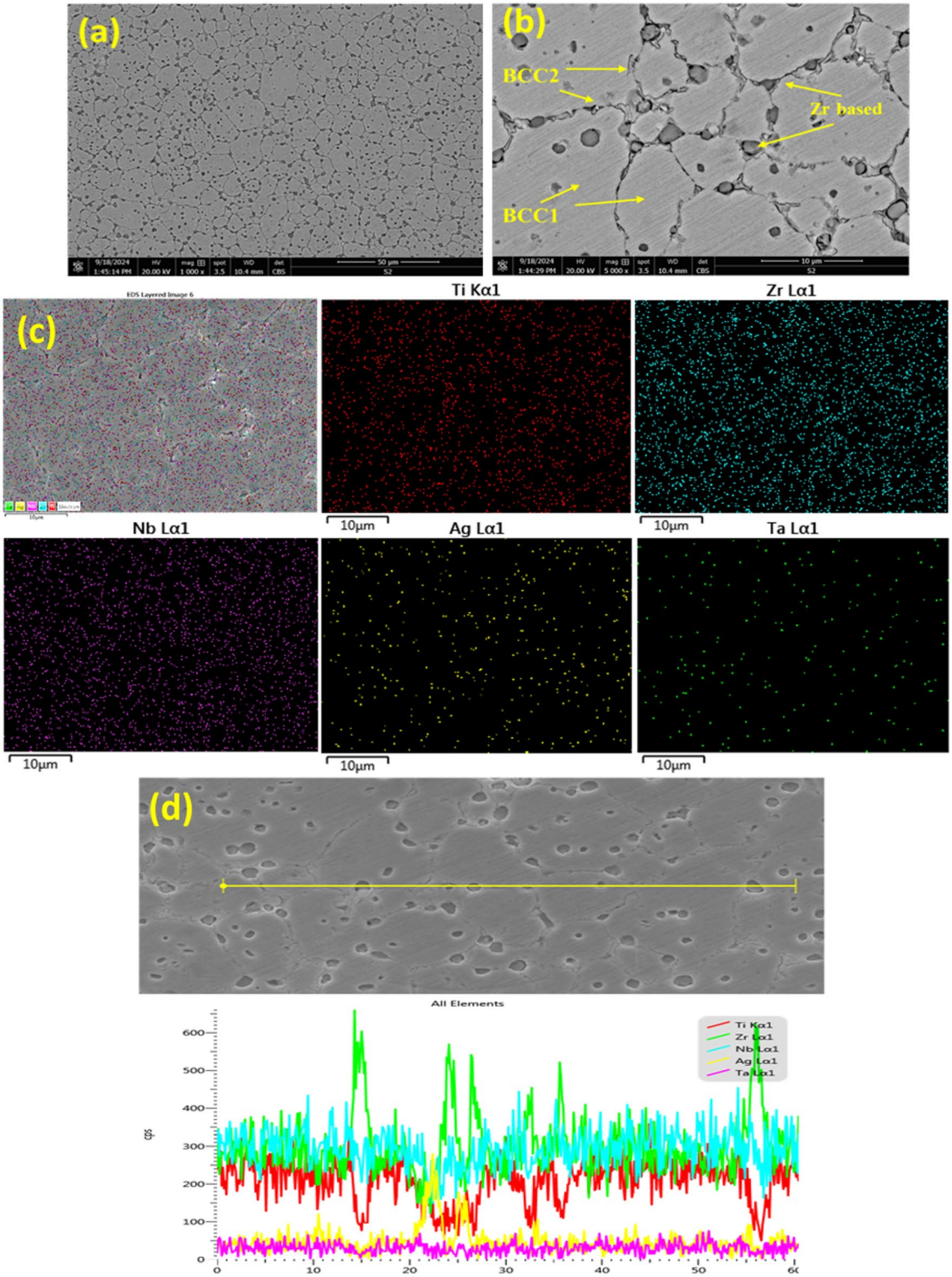

Fig. 3. FE-SEM backscattered images of SPSed HEA at (**a**) Lower and (**b**) Higher magnification showing different phases, (**c**) EDS elemental mapping, and (**d**) Line scan profile.

Wetting characteristics and surface energy measurement

The wettability of the Ti-Zr-Nb-Ta-Ag HEA was determined by measuring the contact angles of the water and glycerol droplets on the polished surface, and the results were compared with those of the Ti6Al4V alloy. The surface energies of the samples were determined using the Owens-Wendt method, which involves measuring the contact angles of two liquids. The contact angles were measured as described elsewhere[51]. The developed HEA had larger contact angles for both water (83.9°) and glycerol (65.1°) than Ti6Al4V (65.41° and 55.96°,

Sample	Hardness (GPa)	Modulus (GPa)	H^3/E^2 (GPa)	Refs.
SPS-HEA	8.20 ± 0.2	132.8 ± 16.3	0.0312	This work
Ti6Al4V	4.11 ± 0.1	141.0 ± 5.1	0.00349	This work
Bio-HEA-1	3.93	87.9 ± 6.31	0.00786	[30]
Bio-HEA-2	5.188	113.26 ± 13.13	0.01089	[30]

Table 1. Hardness and modulus of SPS HEA in comparison to Ti6Al4V alloy and related literature.

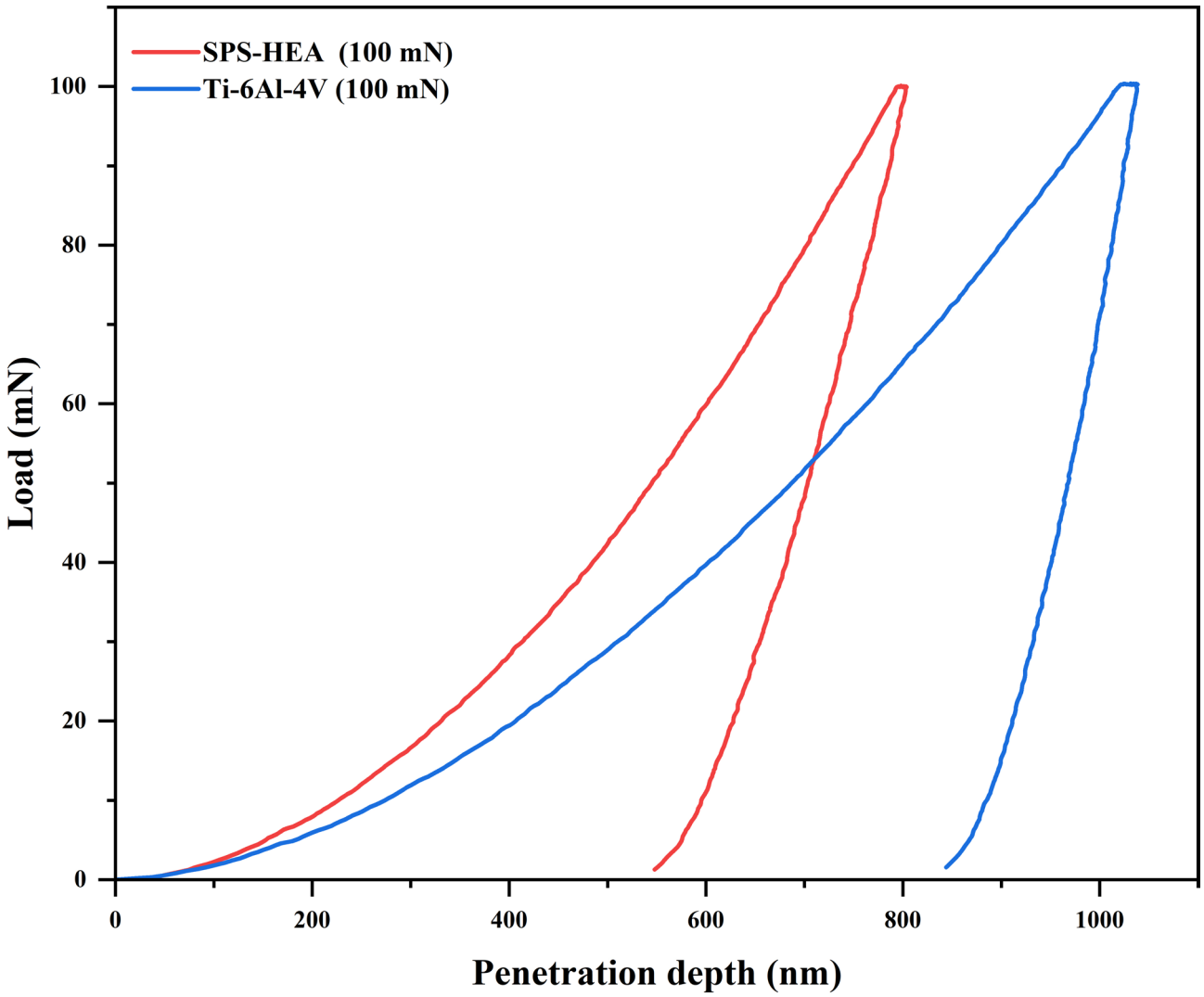

Fig. 4. Loading and unloading curves of SPSed HEA in comparison to Ti6Al4V alloy.

respectively) (Table 2), (droplet images are depicted in Fig. S1), indicating a moderately more hydrophobic surface. This difference in wettability is attributed to the refined microstructure and surface chemistry imparted by the SPS process. Surface energy calculations performed via the Owens-Wendt method confirmed that the HEA possessed a notably lower surface energy (44.25 mN/m) compared to Ti6Al4V (65.93 mN/m). A lower surface energy typically correlates with decreased wettability, which in biomedical contexts can significantly impact protein adsorption and initial cellular responses[52]. Although hydrophilic surfaces are considered favorable for biocompatibility, recent clinical evidence indicates that moderately hydrophobic surfaces have been successfully employed in biomedical implants, demonstrating robust osseointegration[53]. Moreover, surface roughness plays a vital role in mediating dynamic wettability within biological environments. Despite its moderate hydrophobicity, the microscale roughness of HEA (Sa = 0.206 µm) facilitates enhanced protein adsorption owing to the Wenzel effect, significantly reducing the effective contact angle upon exposure to physiological fluids[54]. Importantly, moderate hydrophobicity confers additional clinical advantages, including a reduced risk of bacterial colonization. Surfaces with lower surface energies and modest hydrophobic characteristics can limit bacterial attachment and

Sample	Water contact angle	Glycerol contact angle	Surface energy (mN/m)	Sa (µm)	Sq (µm)	Sv (µm)
HEA-SPS	83.9	65.1	44.25	0.2062	0.2628	2.274
Ti6Al4V	65.41	55.96	65.93	0.4148	0.5049	3.708

Table 2. Contact angle, surface energy, and surface roughness values of SPS-HEA in comparison to Ti6Al4V alloy.

biofilm formation, which are critical factors in reducing peri-implant infections, thereby enhancing implant longevity and clinical outcomes[55]. In addition, hydrophobic surface characteristics are beneficial for corrosion resistance, further contributing to improved implant durability in physiological environments. Furthermore, reduced surface interactions with body fluids can reduce infection concerns, which are critical to implant success. The hydrophobic characteristics also help improve corrosion resistance, which increases the endurance and longevity of the implant. Surface roughness is a critical parameter in biomedical applications that influences cell adhesion, protein adsorption, and biomaterial-tissue interactions.

Figure 5 shows the 3D surface profiles and features of (a) Ti6Al4V and (b) HEA-SPS; the corresponding surface roughness parameters are listed in Table 2. The arithmetic mean height (Sa), root mean square height (Sq), and maximum peak-to-valley height (Sv) were measured following ISO 25,178, which standardizes 3D surface texture characterization. The Sa value of Ti6Al4V is nearly double that of HEA-SPS, suggesting a rougher surface for the former. Surface roughness plays a crucial role in dental implants by affecting cell adhesion and bone integration. Studies have shown that moderate surface roughness (Sa between 0.2 and 1.5 µm) enhances osteoblast attachment and proliferation, which are essential for successful osseointegration[56]. Although Ti6Al4V falls within this range, its higher Sa value could increase the risk of bacterial colonization and biofilm formation, particularly in the oral environment, which is prone to microbial activity[57]. HEA-SPS, with its lower Sa, offers a smoother surface that reduces bacterial adhesion while maintaining sufficient roughness to promote tissue integration. The Sq value of Ti6Al4V was higher than that of HEA-SPS. Sq reflects the standard deviation of the surface heights, emphasizing surface peaks and valleys. For dental implants, the higher Sq values in Ti6Al4V may lead to increased wear under repetitive mechanical loads encountered during chewing. In contrast, the lower Sq value of HEA-SPS suggests a smoother and more uniform surface, which may exhibit superior wear resistance and extend the implant lifespan. Sv was also higher for Ti6Al4V than for HEA-SPS. Higher Sv values in Ti6Al4V indicate more pronounced surface irregularities, which can promote initial mechanical interlocking with bone tissue and enhance the primary stability during the early stages of implantation. However, these pronounced irregularities may act as stress concentration points under cyclic loading, potentially leading to fatigue failures. HEA-SPS, with its lower Sv, provides a smoother interface, reducing stress accumulation and risk of fatigue-related failure. For dental implants, where cyclic forces are continuously applied, a smoother surface can enhance long-term performance. Dental implants are particularly susceptible to bacterial colonization owing to their high microbial load in the oral environment. Rougher surfaces, such as those of Ti6Al4V, offer a greater surface area and microenvironment for bacteria to adhere to and form biofilms. This can lead to peri-implantitis, which is a major cause of implant failure[58]. The lower surface roughness of HEA-SPS, characterized by reduced Sa, Sq, and Sv values, minimized the bacterial adhesion and biofilm formation. This smooth surface enhances its potential for use in infection-prone environments, making it particularly advantageous for dental applications[59,60]. HEA-SPS offers moderate surface roughness, which strikes a balance between promoting bone cell adhesion and reducing the inflammatory response. This is critical for dental implants in which successful osseointegration ensures implant stability and functionality. The smoother surface of HEA-SPS, combined with its biocompatible alloying elements, provides an ideal interface for bone-implant integration while reducing the risk of adverse biological reactions[61]. The superior surface characteristics of HEA-SPS, such as lower Sa, Sq, and Sv, significantly contributed to improved wear resistance, reduced bacterial colonization, and enhanced biomechanical compatibility. These properties are crucial for dental implants, for which durability and resistance to infection are paramount.

X-ray photoelectron spectroscopy analysis

Figure 6 shows the XPS results for the TiZrNbTaAg HEA processed by SPS. XPS data revealed the presence of all five constituent elements (Ti, Nb, Ag, Ta, and Zr), along with carbon and oxygen, on the alloy surface. The presence of oxygen suggests the formation of oxides, such as TiO_2, ZrO_2, Nb_2O_5, and Ta_2O_5 on the alloy surface. These oxides are essential for creating a passivation layer that protects the alloy from degradation in corrosive environments such as the oral cavity. For instance, TiO_2, confirmed by Ti 2p peaks at 458.19 eV, is widely recognized for its role in enhancing biocompatibility and corrosion resistance[62]. This oxide not only shields the alloy from physiological corrosion but also provides an ideal surface for bone cell adhesion, thereby promoting osseointegration[17]. Similarly, Zr 3d peaks at 181.98 eV indicate the formation of ZrO_2, a biocompatible oxide that improves mechanical stability and supports direct bonding with the bone tissue[35]. In addition, the Nb 3d peaks at 206.69 eV confirm the presence of Nb_2O_5, a stable oxide known for its exceptional corrosion resistance and ability to withstand the cyclic loading conditions typical in dental applications. Likewise, the presence of Ta_2O_5, indicated by Ta 4f peaks at 25.56 eV, contributes significantly to the alloy's chemical stability[63]. Tantalum oxides are bioinert and enhance the longevity of implants by protecting against oxidative degradation and ion release, both of which can lead to adverse biological reactions[37]. Furthermore, the XPS results show metallic silver peaks at 364.7 eV and 359.5 eV, with a low atomic percentage (0.28%). Controlled distribution of Ag is advantageous for dental applications. Metallic silver releases Ag^+ ions, which provide potent antimicrobial

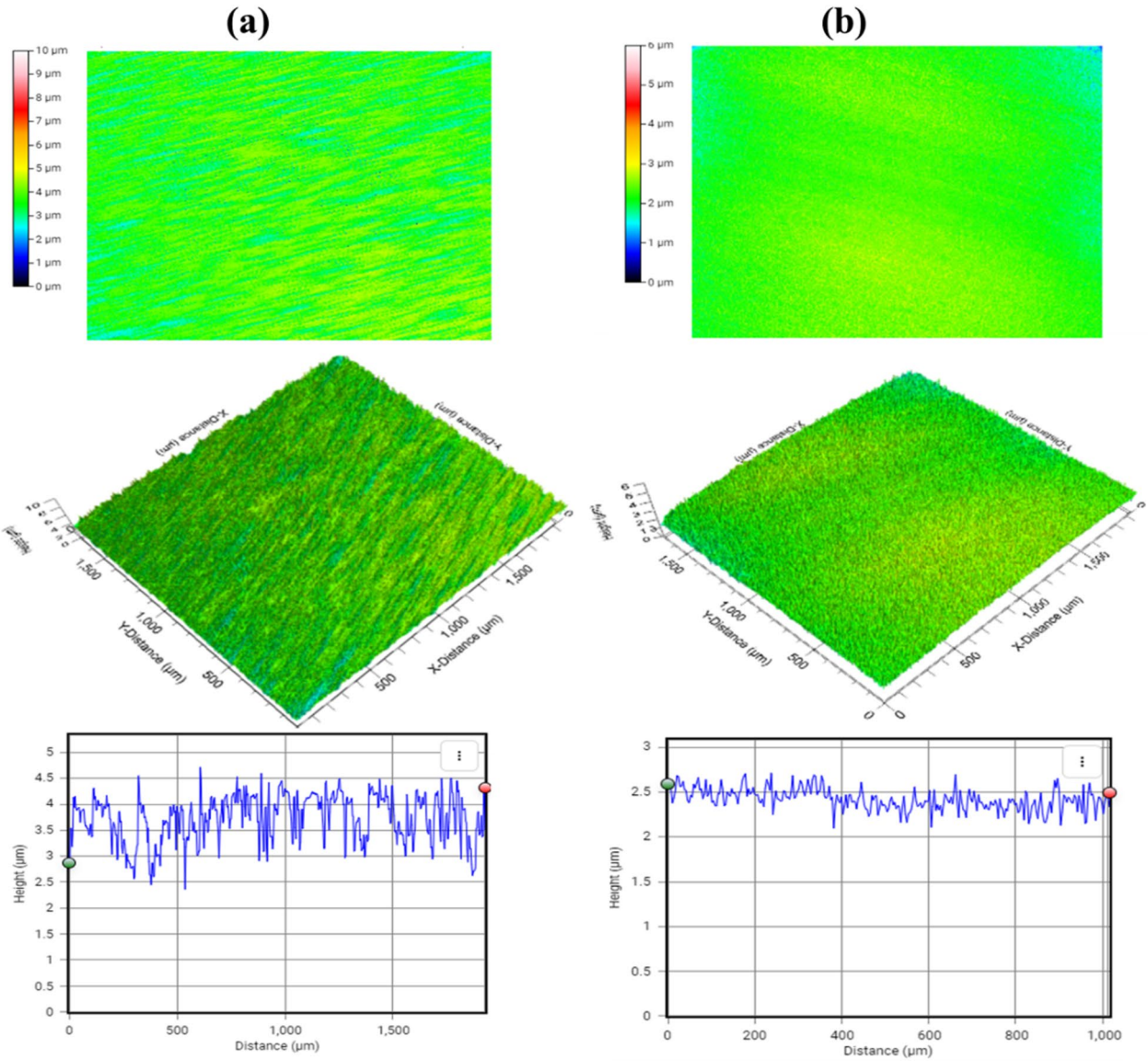

Fig. 5. 3D surface profile and characteristics of (**a**) Ti6Al4V, and (**b**) SPS-HEA.

properties that are essential for preventing bacterial adhesion and biofilm formation. This feature is critical for reducing the risk of peri-implantitis, a common cause of implant failure in dental procedures. Importantly, a low concentration ensures effective antimicrobial action without compromising biocompatibility or inducing cytotoxicity[38]. Despite the tendency of Ag to oxidize, it remained predominantly in its metallic state on the alloy surface. This stability is likely due to the protective oxide layer formed by TiO_2, ZrO_2, Nb_2O_5, and Ta_2O_5, which act as barriers, shielding Ag from environmental oxidation. This unique behavior not only preserves the antimicrobial efficacy of Ag but also maintains the overall chemical stability of the alloy. The detection of carbon in XPS spectra, attributed to surface contamination or hydrocarbon adsorption during handling, is a common observation in XPS studies. This contamination does not detract from the functional properties of the alloy because passivation oxides and metallic silver dominate the surface characteristics that are critical for implant performance. In dental applications, where implants are exposed to a complex oral environment characterized by fluctuating pH, enzymatic activity, and mechanical stress, the surface properties of the TiZrNbTaAg HEA provide distinct advantages. A stable oxide layer ensures excellent corrosion resistance and reduces the risk of material degradation and ion release, which can otherwise lead to inflammatory responses. Additionally, the biocompatibility of oxides, such as TiO_2 and ZrO_2, facilitates effective bone-implant integration, while the antimicrobial properties of silver help mitigate infection risks.

In vitro corrosion study in AS medium

Figure 7(a-f) show the EFM intermodulation curves, which plot the measured current against the investigated frequencies for the SPS-HEA and Ti6Al4V alloys in AS solutions with varying pH levels. The intermodulation and harmonic peaks, with an amplitude of approximately 100 µA, were clearly visible in response to the excitation

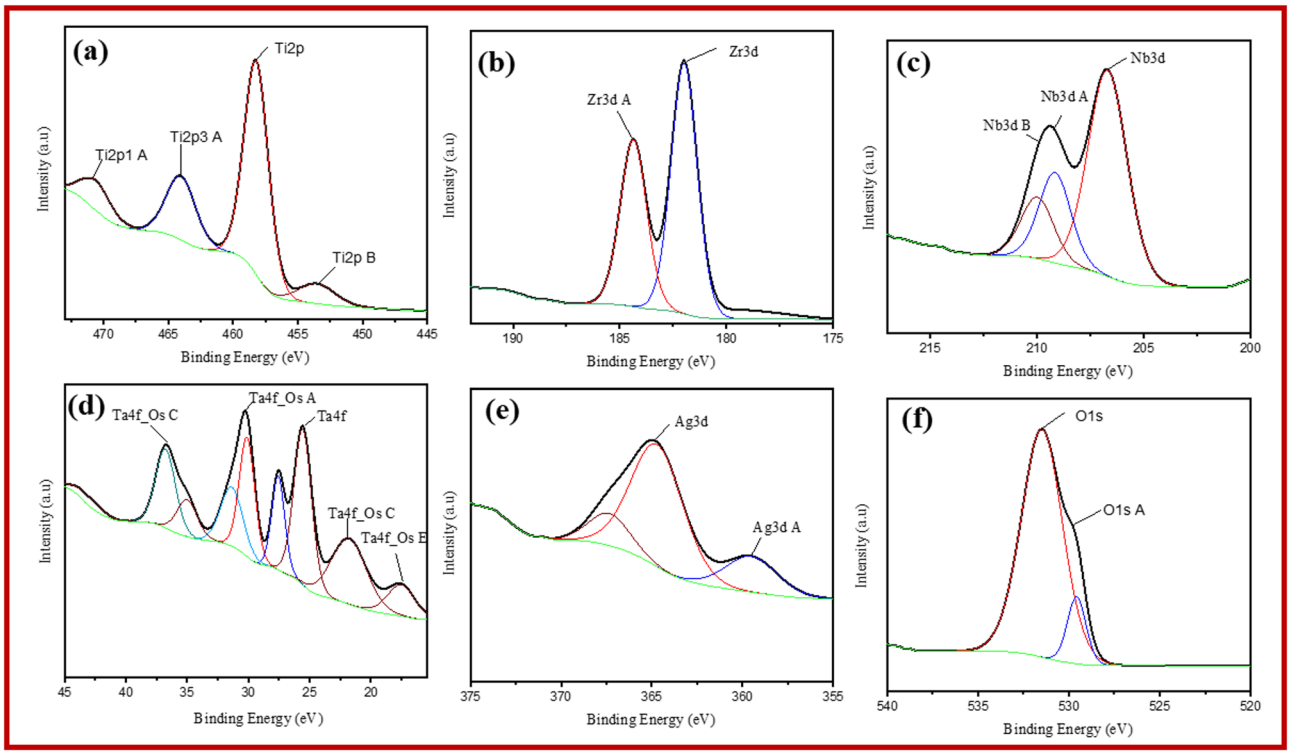

Fig. 6. XPS results for SPS-HEA (**a**) Ti2p, (**b**) Zr3d, (**c**) Nb3d, (**d**) Ta4f, (**e**) Ag3d, and (**f**) O1s.

frequencies (2 and 5 Hz) and were used to calculate the EFM parameters. Table 3 displays the electrochemical parameters, including the corrosion current density (i_{corr}), casualty factors (CF-2 and CF-3), and corrosion rate (CR) for the SPS-HEA and Ti6Al4V alloys. CFs generally validate EFM parameters by ensuring consistency with hypothetical values of 2 and 3, as deviations indicate noise interference[64]. As shown in Table 3, the CF2 and CF3 values are close to the theoretical values, confirming the reliability of the obtained results.

As shown in Table 3, the i_{corr} values for the SPS-HEA alloy remarkably declined by at least one order of magnitude at all the studied pH levels in comparison with those of the Ti6Al4V alloy, signifying the improved corrosion resistance of the SPS-HEA alloy owing to the formation of a compact and inert passive film on its surface. Moreover, the corrosion rate values of the SPS-HEA alloy at different pH values, particularly at pH of 6.8 and 4.9 were found to decrease by one order of magnitude in comparison with the Ti6Al4V alloy, which validated the improved corrosion protection performance of the SPS-HEA alloy in the AS medium.

Figure 8 (a) and (b) show the potentiodynamic polarization curves for the SPS-HEA and Ti6Al4V alloys recorded in AS solutions at varying pH levels. Additionally, the electrochemical parameters, including the corrosion potential (E_{corr}), i_{corr}, and passivation current density (i_{pass}), were determined using the established Tafel method, and the resulting values are presented in Table 3. All the investigated alloys displayed active-passive behavior. The cathodic branches exhibited no notable differences, suggesting that cathodic reactions on the alloy surface remained consistent at different pH levels. A comparison of the E_{corr} values of the Ti6Al4V and SPS-HEA alloys revealed that the SPS-HEA alloy had a higher E_{corr} than Ti6Al4V. This indicates that the SPS-HEA alloy had a more positive E_{corr} value, thus exhibiting superior corrosion resistance in the AS medium at pH 6.8. The SPS-HEA alloy exhibited the lowest i_{pass}, whereas the Ti6Al4V alloy exhibited the highest i_{pass}. Corrosion resistance is better when i_{corr} and/or CR, as well as i_{pass}, are low[65]. Considering all these parameters, it is evident that the SPS-HEA alloy immersed in AS at pH 6.8 demonstrates the highest corrosion resistance, with the lowest i_{corr} and i_{pass} values when compared to the other commercial alloys. This behavior can be attributed to the microstructure of the SPS-HEA alloy, where the synergistic strengthening effects of elements such as Nb, Ta, and Zr, along with unique phase interactions, promote the formation of a spontaneous passive film[66]. This in turn shifts the corrosion potential to more noble values.

The effect of the pH on the AS solution revealed a significant decline in the corrosion resistance of the investigated Ti alloys. In particular, at pH 3.0, the corrosion resistance of the Ti6Al4V alloy is significantly diminished, and the passive film provides inadequate protection to the underlying matrix[67]. In contrast, the SPS-HEA alloy exhibited substantial corrosion resistance, which was attributed to the stabilizing effects of Nb and Zr oxides on the passive films. In general, HEA alloys containing Nb, Zr, and Ta demonstrate excellent corrosion resistance compared with CP-Ti and Ti6Al4V alloys in acidic fluoride-containing environments[67], highlighting their promising potential for advancements in the field of bio-implants.

Electrochemical impedance spectroscopy (EIS) tests were conducted to analyze the electrochemical behavior at the interfaces of the solution, oxide layer, and matrix of the investigated samples at their open-circuit potentials (OCPs). The results presented in Fig. 9 (a-b) depict the Bode diagrams of the Ti6Al4V and SPS-HEA alloys in AS

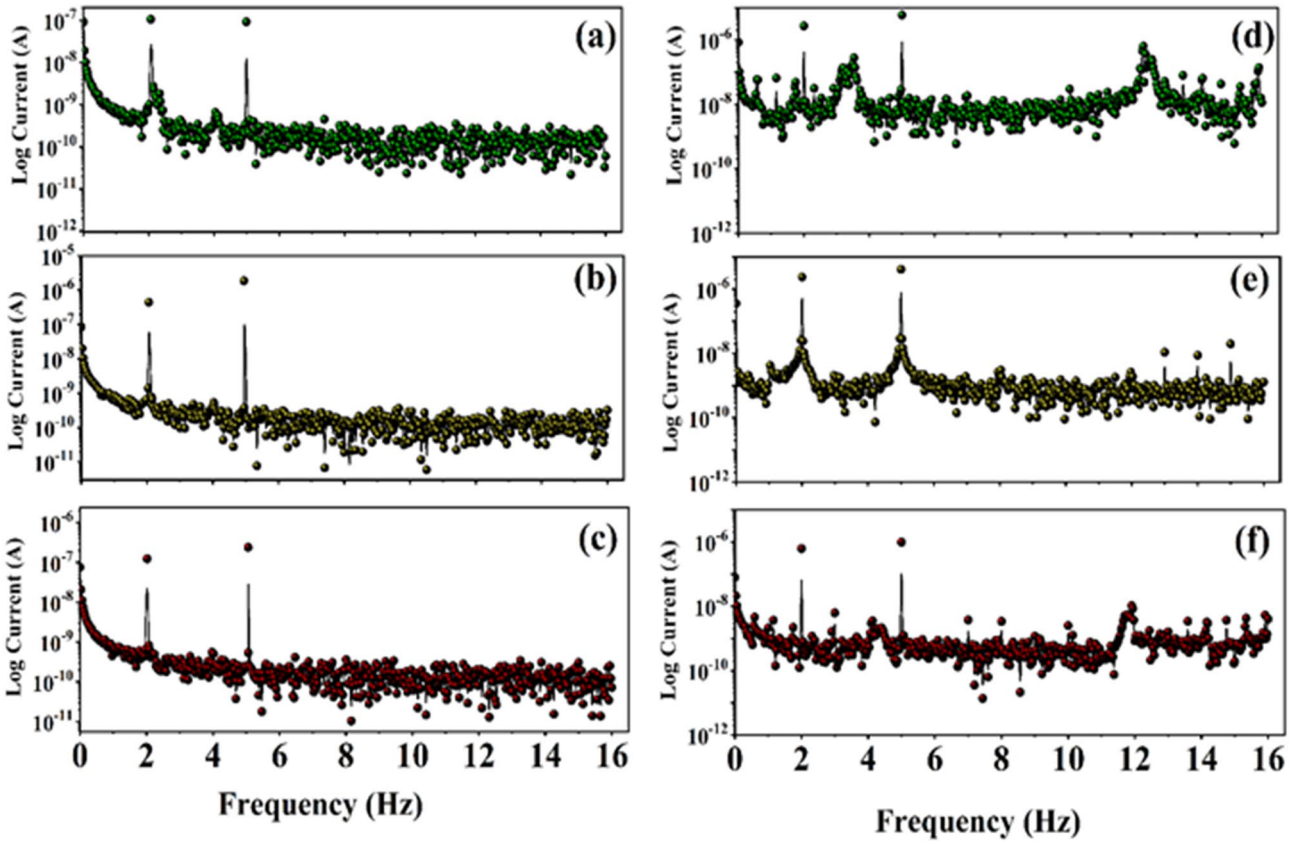

Fig. 7. EFM curves of (**a**) pH6.8, (**b**) pH4.9, (**c**) pH3.0 of SPS HEA alloys and (**d**) pH6.8, (**e**) pH4.9 and (**f**) pH3.0 of Ti6Al4V alloy in AS medium.

Samples/test	EFM				PDP		
	i_{corr} (A cm^{-2}) × 10^{-8}	CF2	CF3	CR (mpy) × 10^{-3}	E_{corr} (V)	i_{corr} (A cm^{-2}) × 10^{-8}	i_{pass} (A cm^{-2}) × 10^{-8}
SPS HEA							
pH-6.8	0.101	1.89	2.85	0.345	0.217	0.1842	2.128
pH-4.9	0.118	1.87	2.84	0.381	0.031	1.254	18.880
pH-3.0	1.348	1.87	2.81	4.662	-0.191	2.358	106.489
Ti6Al4V							
pH-6.8	0.834	1.90	2.87	2.881	-0.168	1.076	14.825
pH-4.9	1.230	1.88	2.84	4.252	-0.104	2.584	60.891
pH-3.0	8.764	1.88	1.79	30.305	-0.186	10.251	1227.145

Table 3. EFM and PDP parameters of SPS HEA in AS medium with different pH levels in comparison to Ti6Al4V alloy (The standard deviation of the obtained values was found to range between 0.75% and 5.25%).

solutions with varying pH levels. The SPS-HEA alloy demonstrated enhanced impedance at lower frequencies and exhibited nonideal capacitive behavior, as reflected by a phase angle greater than − 80° (Fig. 9a). In the Bode plots (Fig. 9a), the modulus of impedance ($|Z|$) of the SPS-HEA alloy is higher than that of the Ti6Al4V alloy, indicating an enhancement in the corrosion resistance of the protective oxide layer on the SPS-HEA alloy in the AS solution. Furthermore, the SPS-HEA alloy exhibited the largest phase angle (− 85°) compared with the Ti6Al4V alloy (− 75°), suggesting the presence of a more protective passive film on the SPS-HEA alloy in the AS solution at pH 6.8.

Nyquist plots of the Ti6Al4V and SPS-HEA alloys in AS solutions with varying pH levels are presented in Fig. 10 (a-f). At pH 3.0, the Nyquist plot of the Ti6Al4V substrate exhibited a capacitive semicircular arc, whereas the HEA substrates showed a capacitive arc with a linear trend, suggesting that the passive films on the HEA alloys effectively impeded charge transfer at the metal–electrolyte interface. The distinct quarter-arcs observed in the Nyquist plots of the investigated samples at different pH values in Fig. 10 indicate capacitive behavior, with their radii reflecting the level of corrosion resistance. The radii of the semicircular arcs are

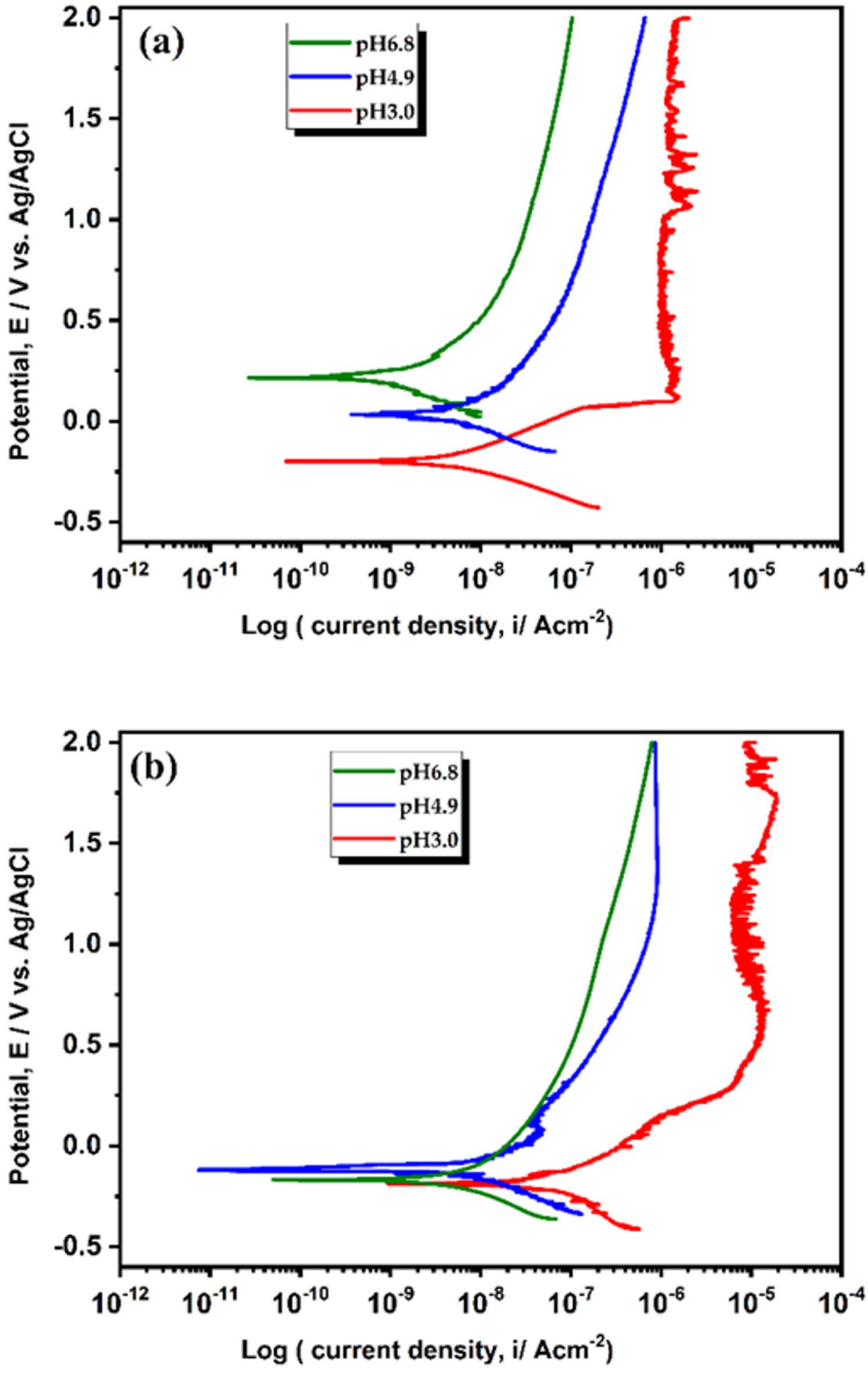

Fig. 8. PDP curves of (**a**) SPS-HEA and (**b**) Ti6Al4V alloys in AS with different pH levels.

directly associated with the charge-transfer resistance, which in turn is directly related to the corrosion rate of the material. Therefore, an increase in the polarization resistance corresponded to a decrease in the corrosion rate. Accordingly, the SPS-HEA samples exhibited larger capacitive arcs across all studied pH levels, indicating lower corrosion kinetics compared to the Ti alloy.

The Bode plots revealed that the Ti6Al4V alloy in the AS solution had the lowest impedance and phase angle at pH 3.0, indicating the highest corrosion kinetics. In contrast, the SPS-HEA samples exhibited higher impedance and phase angles, suggesting lower corrosion kinetics than the Ti6Al4V alloy.

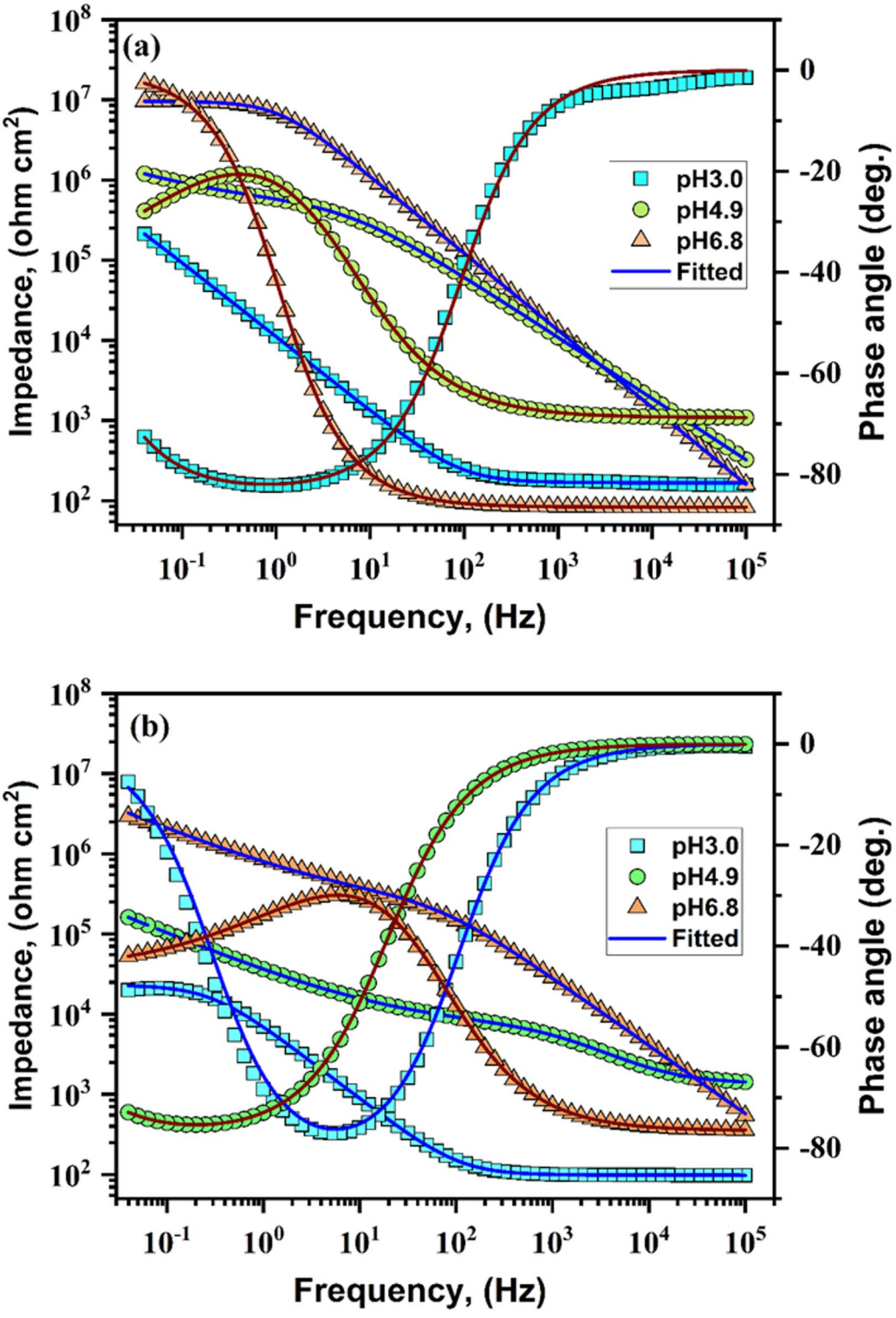

Fig. 9. Bode curves of (**a**) SPS-HEA and (**b**) Ti6Al4V alloys in AS with different pH levels.

Based on this analysis, two equivalent circuits were employed to quantify the differences in the physicochemical behaviors of the Ti6Al4V and SPS-HEA alloys in AS at different pH values, as illustrated in Fig. 11 (a-b). For pH 3.0, the circuit model in Fig. 11a was used to fit the obtained EIS curves, whereas for pH 4.9 and pH 6.8, the circuit model in Fig. 11b was used. These circuits primarily consist of resistance components (R) and constant-phase elements (CPE). In this study, CPEs were used instead of capacitors to account for the distribution of relaxation times, as the surface heterogeneity of the electrodes influences the charge-transfer capacity and capacitance of the passive film at the metal–electrolyte interface[68]. The extracted parameter values are listed

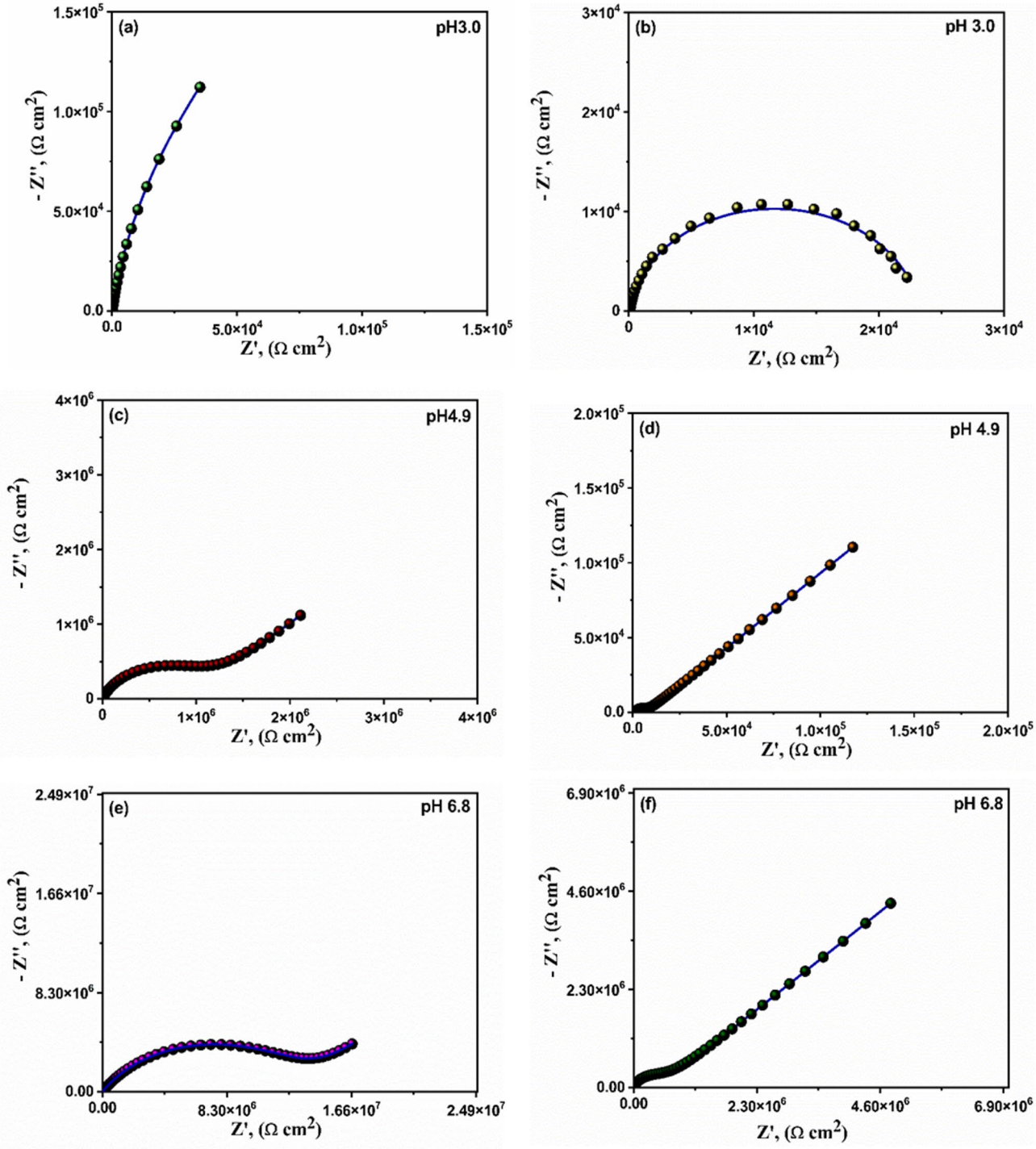

Fig. 10. Nyquist plots of (**a**) SPS-HEA in pH3.0, (**b**) Ti6Al4V in pH3.0, (**c**) SPS-HEA in pH4.9, (**d**) Ti6Al4V in pH4.9, (**e**) SPS-HEA in pH6.8, and (**f**) Ti6Al4V in pH6.8.

in Table 4. The Chi-squared (χ^2) values for all samples are of the order of 10^{-5}, indicating excellent agreement between the experimental data and the fitting results.

As shown in Table 4, the R_{ct} values of the investigated samples decreased with decreasing pH of the AS solution. Furthermore, under normal human oral conditions (pH 6.8), the SPS-HEA alloy exhibited the highest R_{ct} value (1.0805×10^7 Ω·cm²) and lowest CPEdl value (0.085 $\mu\Omega^{-1}\cdot cm^{-2}\cdot sn$), indicating the formation of a dense passivation film on its surface. At pH 3.0, the R_{ct} value of Ti6Al4V was on the order of 10^{-4}, suggesting that the passive film formed on the surface of the Ti6Al4V alloy exhibited poor stability at higher H + concentrations as the pH value decreased.

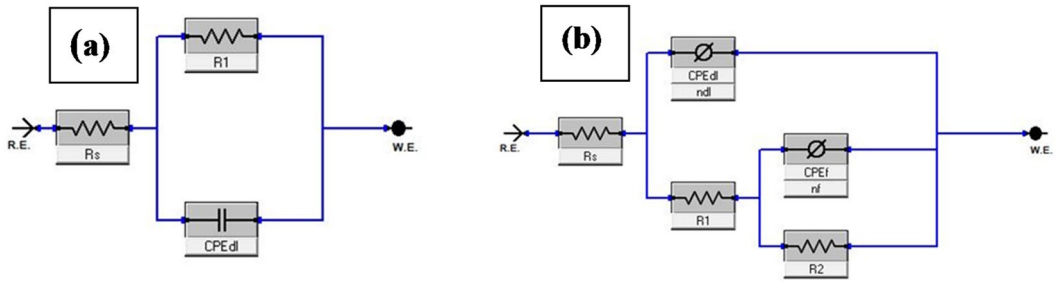

Fig. 11. EIS circuit models for the Ti6Al4V and SPS-HEA alloys in AS medium in different pH, (**a**) pH3.0 and (**b**) pH 4.9 and pH6.8.

Samples/test	R_s ($\Omega \cdot cm^2$)	R_{ct} ($k\Omega \cdot cm^2$)	CPE_{dl} ($\mu\Omega^{-1} \cdot cm^{-2} \cdot s^n$)	n_{dl}	$\chi^2 \times 10^{-5}$
SPS HEA					
pH-6.8	56.58	10805.083	0.085	0.96	1.586
pH-4.9	48.58	1241.654	0.254	0.90	3.589
pH-3.0	52.38	216.000	1.589	0.87	2.568
Ti6Al4V					
pH-6.8	58.26	3179.083	0.485	0.94	5.684
pH-4.9	55.21	169.534	1.894	0.91	2.548
pH-3.0	51.24	19.481	10.258	0.87	6.981

Table 4. EIS parameters of investigated alloys in AS medium with different pH levels (The standard deviation of the obtained values was found to range between 0.75% and 5.25%).

At pH 4.9, the R_{ct} values of the Ti6Al4V alloy were significantly lower than those of the SPS-HEA. At pH 3.0, the R_{ct} value of the Ti6Al4V alloy was at least one order of magnitude smaller than that of the SPS-HEA alloy, indicating significant damage to the passive films on the surface of the Ti6Al4V alloy, leading to the corrosion of the metal matrix. In contrast, the higher Rct values of the SPS-HEA alloy suggest that the passive film on this alloy provided better protection, which can be attributed to the stable oxides of Nb, Zr, and Ta.

In summary, the comprehensive evaluation of the Ti–Zr–Nb–Ta–Ag HEA developed via MA and SPS demonstrates its combined mechanical, surface, and in vitro corrosion performance in artificial saliva, highlighting its potential for dental biomaterial applications. The elastic modulus was measured to be approximately 132 GPa. Although this value is slightly higher than that of commercially pure titanium (~ 110 GPa)[69], it remains significantly lower than those of conventional dental alloys, such as cobalt–chromium (Co–Cr, ~ 210–253 GPa) and stainless steel (~ 190 GPa)[69], which are still commonly used in clinical practice. More importantly, the developed HEA exhibited a synergistic combination of desirable properties, including high hardness (8.2 GPa), resistance to plastic deformation ($H^3/E^2 = 0.0312$ GPa), and outstanding corrosion resistance across a wide range of pH values in artificial saliva, compared to the Ti6Al4V alloy. These features, along with the formation of a chemically stable and biocompatible passive oxide layer composed of TiO_2, ZrO_2, Nb_2O_3, Ta_2O_3, and metallic Ag, are expected to promote long-term mechanical durability, biological compatibility, and osseointegration. Collectively, these results suggest that SPS-processed HEA are promising candidates for next-generation dental bioimplants.

Future work should focus on further optimizing the elastic modulus and reducing potential stress shielding. This may be achieved through compositional adjustments, such as increasing the β-phase stabilizing elements and refined control of microstructural features via advanced processing strategies. Additionally, the introduction of controlled porosity through processing could effectively lower the effective modulus without compromising the mechanical integrity or surface functionality of the alloy. These combined approaches aim to enhance the biomechanical compatibility of the developed HEA while retaining its favorable electrochemical and biological performance, thereby advancing its translational potential in clinical dental applications.

Conclusion

This study reports the synthesis of Ti-Zr-Nb-Ta-Ag HEA via mechanical alloying and SPS and evaluates its potential for dental bioimplant applications. A thorough examination of the phase composition, microstructure, mechanical properties, surface characteristics, and corrosion resistance of the alloys is summarized below.

1. Microstructure analyses reveal the formation of a homogeneous microstructure with dual phases BCC structure and an equiaxed Zr-rich phase using the SPS process.
2. The micro hardness of SPS-ed HEA is 8.2 GPa, nearly double that of Ti6Al4V (4.11 GPa).
3. Surface characterization using XPS revealed the formation of surface oxides of TiO_2, ZrO_2, Nb_2O_5, and Ta_2O_5 alongside Ag.

4. In vitro corrosion testing results in artificial saliva confirmed that the SPSed HEA alloy outperformed Ti6Al4V in terms of corrosion resistance, even at acidic pH, by showing higher impedance values and lower corrosion current densities.
5. These findings highlight that the combination of the mechanical strength of the SPS-ed Ti-Zr-Nb-Ta-Ag HEA and enhanced in vitro corrosion resistance demonstrates its suitability as a promising candidate for dental bioimplant applications.

Future studies should focus on the in vivo evaluation and long-term performance assessment of the developed HEA under real oral conditions.

Data availability

Data availability statementThe data will be available upon reasonable request from corresponding author.

Received: 8 January 2025; Accepted: 18 August 2025
Published online: 26 September 2025

References

1. Hussein, M. A., Madhan Kumar, A., Azeem, M. A., Sorour, A. A. & Saravanan, S. Ti–30Nb–3Ag alloy with improved corrosion resistance and antibacterial properties for orthopedic and dental applications produced by mechanical alloying. *J. Mech. Behav. Biomed. Mater.* **142**, 105851 (2023).
2. Xu, D., Wang, X. & Lu, Y. Heterogeneous-Structured refractory High-Entropy alloys: A review of State-of-the-Art. *Developments Trends Adv. Funct. Mater.* 2408941. (2024).
3. Xiong, W., Guo, A. X. Y., Zhan, S., Liu, C. T. & Shan Cecilia Cao. Refractory high-entropy alloys: A focused review of Preparation methods and properties. *J. Mater. Sci. Technol.* **142**, 196–215 (2023).
4. Krishna, S., Aravind, N., Noble, N., Radhika & Saleh, B. A comprehensive review on advances in high entropy alloys: fabrication and surface modification methods, properties, applications, and future prospects. *J. Manuf. Process.* **109**, 583–606 (2024).
5. Wang, S. P. & Xu, J. TiZrNbTaMo high-entropy alloy designed for orthopedic implants: As-cast microstructure and mechanical properties. *Mater. Sci. Engineering: C.* **73**, 80–89 (2017).
6. Yuan, Y. et al. Formation, structure and properties of biocompatible TiZrHfNbTa high-entropy alloys. *Mater. Res. Lett.* **7** (6), 225–231 (2019).
7. Nguyen, V. T. et al. A novel quaternary equiatomic Ti-Zr-Nb-Ta medium entropy alloy (MEA). *Intermetallics* **101**, 39–43 (2018).
8. Chen, Y. L. et al. Competition between elements during mechanical alloying in an octonary multi-principal-element alloy system. *J. Alloys Compd.* **481** (1–2), 768–775 (2009).
9. Zhang, K. B. et al. Nanocrystalline cocrfenicual high-entropy solid solution synthesized by mechanical alloying. *J. Alloys Compd.* **485**, 1–2 (2009).
10. Arun, S. & Radhika, N. and Bassiouny Saleh. Advances in vacuum Arc melting for high entropy alloys. *Rev. Vacuum* 113314. (2024).
11. Zhang, L. et al. Xin lu, and Yanhao dong. Powder metallurgy route to ultrafine-grained refractory metals. *Adv. Mater.* **35** (50), 2205807 (2023).
12. Hussein, M. A., Suryanarayana, C. & Al-Aqeeli, N. Fabrication of nano-grained Ti–Nb–Zr biomaterials using spark plasma sintering. *Mater. Design*. **87**, 693–700 (2015).
13. Srivastav, C., Kumar, N., Sai Anuraag, A. K. & Pandey Nand Kishore prasad, and Debashis khan. Design, Preparation and study of microstructure, phase evolution and thermal stability of Ti-Co0. 35-Cr0. 35-Nb-Zr nanocrystalline HEA for biomedical applications. *Mater. Today Commun.* **35**, 105557 (2023).
14. Yousefi, M., Rajabi, M. & Reyhani, A. and Nayereh Asgari. Corrosion and biocompatibility properties of tizrnbcrv, tizrnbfecr, and TiZrNbFeV high entropy alloys produced through mechanical alloying. *J. Mater. Eng. Perform*. 1–13. (2023).
15. Du, P. et al. Optimizing the cell compatibility and mechanical properties in TiZrNbTa medium-entropy alloy/β-Ti composites through phase transformation. *Acta Biomater.* **181**, 469–482 (2024).
16. Hussein, M. A. Synthesis, characterization, and surface analysis of near-β Ti20Nb20Zr alloy proceeded by powder metallurgy for biomedical applications. JOM 74, no. 3 924–930. (2022).
17. Hu, Z. Y. et al. A review of multi-physical fields induced phenomena and effects in spark plasma sintering: fundamentals and applications. *Mater. Design*. **191**, 108662 (2020).
18. Ralls, A. M., Daroonparvar, M. & Menezes, P. L. Spark plasma sintering of Mg-based alloys: microstructure, mechanical properties, corrosion behavior, and tribological performance. *J. Magnesium Alloys*. **12**, 405–442 (2024).
19. Unversity, K. A. Y. et al. Khoja Akhmet Yassawi Unversity, A Brief Overview Of The Technology Of Spark Plasma Sintering Of Functional Materials For Practical Purpose, Easktu 4 57–66. (2024).
20. Jayasree, R. et al. Bi-layered metal-ceramic component for dental implants by spark plasma sintering. *Mater. Lett.* **344**, 134403 (2023).
21. Moayedee, Y., Nikzad, L. & Majidian, H. Exploration into the microstructural, mechanical, and biological characteristics of the functionally graded 3Y-TZP/Ti6Al4V system as a potential material for dental implants. *J. Mech. Behav. Biomed. Mater.* **151**, 106380 (2024).
22. Ma, Li, Y., Li, C., Wang, Z., Chen, S. & Zhao Bo cheng, and Cheng-lin li. Bioactive Zn ingredients endow Ti-Zn composites with exceptional mechanical and osteogenic properties as biomedical implants. *Biomaterials Adv.* **174**, 214308 (2025).
23. Al-Sayaad, Y. et al. Analytical study to effects on reflection coefficient of Ti–Mn alloys at increasing concentration Mn element in the dental implants application. *J. Mech. Behav. Biomed. Mater.* **143**, 105920 (2023).
24. Lu, X. et al. Microstructure and mechanical properties of spark plasma sintered Ti-Mo alloys for dental applications. *Int. J. Minerals Metall. Mater.* **21** (5), 479–486 (2014).
25. Kondo, H. et al. Motohiro uo, and Takao kawasaki. Fabrication of titanium nitride/apatite functionally graded implants by spark plasma sintering. *Mater. Trans.* **45** (11), 3156–3162 (2004).
26. Gali, S., Gururaja, S., Prabhu, T. N. & Srinivasan, S. Investigation of spark plasma sintering on Microstructure-Properties of zirconia reinforced fluormica glass for dental restorations. *Mater. (Basel).* **16** (18), 6125. https://doi.org/10.3390/ma16186125 (2023). PMID: 37763404; PMCID: PMC10532871.
27. Jiang Tao, W., Haochen, F., Shaoli, C. & Xiaohong *Liu Ping,Recent Progress in Fabrication, Element Addition and Surface Modification of TiZr Materials in Dental implants,Journal* (of Materials Research and Technology, 2025).
28. Razumov, N., Makhmutov, T., Kim, A. & Popovich, A. Structure and properties of High-Entropy boride ceramics synthesized by mechanical alloying and spark plasma sintering. *Materials* **16**, 6744 (2023).

29. Naser-Zoshki, H., Kiani-Rashid, A. R. & Vahdati-Khaki, J. Non-equiatomic W10 Mo27 Cr21 Ti22 Al20 high-entropy alloy produced by mechanical alloying and spark plasma sintering: Phase evolution and mechanical properties, Proceedings of the Institution of Mechanical Engineers, Part L: Journal of Materials: Design and Applications 236 695–703. (2022).
30. Hussein, M. A., Kumar, A. M., Azeem, M. A., Ankah, N. & Saravanan, S. Development of Ti-Zr-Nb-Ta-Ag high entropy alloy for dental implants: in vitro corrosion behavior, antibacterial activity, and surface characteristics. *Mater. Chem. Phys.* **329**, 130114 (2025).
31. Roegnitz, A. & Haeger, A. The tribological behaviour of titanium alloys suitable for dental implants: A short review. *Curr. Dir. Biomedical Eng.* **10**, 530–534 (2024).
32. Moghanian, A. & Nasiripour, S. Bioinert Ceramics for Biomedical Applications, in: S. Kargozar, F. Baino (Eds.), Bioceramics: Status in Tissue Engineering and Regenerative Medicine (Part 1), BENTHAM SCIENCE PUBLISHERS, : pp. 103–124. (2024).
33. Singh, G., Singh Sidhu, B. & Singh, B. A Review of Utilization of Niobium and Tantalum for the Enhancement in Corrosion Resistance and Biocompatibility of Bio-Implants, in: A. Agarwal, G. Bolelli, A. Concustell, Y.-C. Lau, A. McDonald, F.-L. Toma, E. Turunen, C.A. Widener (Eds.), Düsseldorf, Germany, : pp. 814–824. (2017).
34. Dercz, G. et al. Effect of Nb and Zr alloying additives on structure and properties of Ti-Ta-Nb-Zr alloys for medical applications. *Arch. Metall. Mater.* 1467–1472. (2024).
35. Oliver, W. C. & Pharr, G. M. Measurement of hardness and elastic modulus by instrumented indentation: advances in Understanding and refinements to methodology. *J. Mater. Res.* **19**, 3–20 (2011).
36. Li, Z., Liang, D., Zhong, C., Wan, T. & Zhu, W. Jiasi luo,jianfeng yan, Fuzeng ren, comprehensive evaluation of corrosion resistance and biocompatibility of ultrafine-grained TiMoNb alloy for dental implants. *J. Mater. Sci. Technol.*, (2024). ISSN 1005 – 0302.
37. Suryanarayana, C. Mechanical alloying and milling. *Prog. Mater. Sci.* **46** (1–2), 1–184 (2001).
38. Sivasankaran, S., Sivaprasad, K., Narayanasamy, R. & Satyanarayana, P. V. X-ray peak broadening analysis of AA 6061100 – x– x wt.% Al2O3 nanocomposite prepared by mechanical alloying. *Mater. Charact.* **62** (7), 661–672 (2011).
39. Nguyen, V. T. et al. Cuboid-like nanostructure strengthened equiatomic Ti–Zr–Nb–Ta medium entropy alloy. *Mater. Sci. Engineering: A*. **798**, 140169 (2020).
40. Hussein, M. A., Azeem, A., Kumar, M. & Ankah, N. A. M., Design and development of Ti–Zr–Nb–Ta–Ag high entropy alloy for bioimplant applications. *Adv. Eng. Mater.*, 2400462 .
41. Yeh, J. W. Alloy design strategies and future trends in high-entropy alloys. *JOM* **65**, 1759–1771 (2013).
42. Hanawa, T. Research and development of metals for medical devices based on clinical needs. *Sci. Technol. Adv. Mater.* 13 (2012).
43. Geetha, M., Singh, A. K., Asokamani, R. & Gogia, A. K. Ti based biomaterials, the ultimate choice for orthopaedic implants - A review. *Prog Mater. Sci.* **54**, 397–425 (2009).
44. Niinomi, M. & Nakai, M. Titanium-based biomaterials for preventing stress shielding between implant devices and bone, Int J Biomater (2011). (2011).
45. Hussein, M. A., Madhan Kumar, A., Yilbas, B. S. & Al-Aqeeli, N. Laser nitriding of the newly developed Ti-20Nb-13Zr at.% biomaterial alloy to enhance its mechanical and corrosion properties in simulated body fluid. *J. Mater. Eng. Perform.* **26**, 5553–5562 (2017).
46. Kim, K. T., Eo, M. Y., Nguyen, T. T. H. & Kim, S. M. General review of titanium toxicity. *Int. J. Implant Dent.* **5** (2019).
47. Yeh, J. W. et al. Nanostructured high-entropy alloys with multiple principal elements: novel alloy design concepts and outcomes. *Adv. Eng. Mater.* **6**, 299–303 (2004).
48. Khadija, G. et al. Short term exposure to titanium, aluminum and vanadium (Ti 6Al 4V) alloy powder drastically affects behavior and antioxidant metabolites in vital organs of male albino mice. *Toxicol. Rep.* **5**, 765–770 (2018).
49. Tsai, M., Yeh, J. & Alloys, H. E. *Crit. Rev. High-Entropy Alloys: Crit. Rev.* **2**.3 107–123. (2014).
50. Besinis, A., Hadi, S. D., Le, H. R., Tredwin, C. & Handy, R. D. Antibacterial activity and biofilm Inhibition by surface modified titanium alloy medical implants following application of silver, titanium dioxide and hydroxyapatite nanocoatings. *Nanotoxicology* **11**, 327–338 (2017).
51. Hussein, M. A., Yilbas, B., Madhan Kumar, A., Drew, R. & Al-Aqeeli, N. Influence of laser nitriding on the surface and corrosion properties of Ti-20Nb-13Zr alloy in artificial saliva for dental applications. *J. Mater. Eng. Perform.* **27**, 4655–4664 (2018).
52. Gittens, R. A. et al. A review on the wettability of dental implant surfaces II: biological and clinical aspects. *Acta Biomater.* **10**, 2907–2918 (2014).
53. Lang, N. P. et al. Early osseointegration to hydrophilic and hydrophobic implant surfaces in humans. *Clin. Oral Implants Res.* **22**, 349–356 (2011).
54. Vogler, E. A. Protein adsorption in three dimensions erwin. *Bone* **23**, 1–7 (2013).
55. Zheng, S. et al. Implication of surface properties, bacterial motility, and hydrodynamic conditions on bacterial surface sensing and their initial adhesion. *Front. Bioeng. Biotechnol.* **9**, 1–22 (2021).
56. Wennerberg, A. & Albrektsson, T. Effects of titanium surface topography on bone integration: A systematic review, clin. *Oral Implants Res.* **20**, 172–184 (2009).
57. Cordeiro, J. M. et al. Development of binary and ternary titanium alloys for dental implants. *Dent. Mater.* **33**, 1244–1257 (2017).
58. Chun Giok, K. & Menon, R. K. The Microbiome of Peri-Implantitis: A systematic review of Next-Generation sequencing studies. *Antibiotics* **12**, 1–30 (2023).
59. Sista, S., Wen, C., Hodgson, P. D. & Pande, G. The influence of surface energy of titanium-zirconium alloy on osteoblast cell functions in vitro. *J. Biomed. Mater. Res. - Part. A*. **97 A**, 27–36 (2011).
60. Deligianni, D. D. et al. Effect of surface roughness of the titanium alloy Ti-6Al-4V on human bone marrow cell response and on protein adsorption. *Biomaterials* **22**, 1241–1251 (2001).
61. Huang, H. H. et al. Surface nanoporosity of β-type Ti-25Nb-25Zr alloy for the enhancement of protein adsorption and cell response. *Surf. Coat. Technol.* **259**, 206–212 (2014).
62. Liu, Y. et al. Surface & coatings technology microstructure and properties of novel nano-lamellar Ti-6Al-4V alloy, 492 131188. (2024).
63. Kuroda, P. A. B. et al. Influence of Zr addition in β Ti-25Ta-xZr alloys on oxide formation by. *Vacuum* **217**, 112541 (2023).
64. Hussein, M. A., Madhan Kumar, A., Ankah, N. & Azeem, M. A. Thermal treatment effect on the surface and in vitro corrosion characteristics of Arc deposited TiN coating on Ti alloy for orthopedic applications. *Ceram. Int.* **47**, 23203–23213 (2021).
65. Ibrahim, H., Elshamy, Magdy, A. M., Ibrahim, Sayed, S., Abdel Rehim, Nobl, F. & El Boraei Electrochemical characteristics of a biomedical Ti70Zr20Nb7.5Ta2.5Refractory high entropy alloy in an artificial saliva solution. *J. Bio- Tribo-Corrosion*. **9**, 10 (2023).
66. Vitelaru, C. et al. Corrosion behaviour of Ti6Al4V alloy in artificial saliva solution with fluoride content and low pH value. *Mat. Wiss Werkstofftech*. **45** (2), 91–98 (2014).
67. Lin, H., Zhang, G., Chen, W., Zheng, K. & Yin, F. Design of new β-type Ti alloys with outstanding corrosion and wear resistance for dental application. *Corros. Sci.* **241**, 112520 (2024).
68. Carnot, A. et al. Corrosion mechanisms of steel concrete moulds in contact with a demoulding agent studied by EIS and XPS. *Corros. Sci.* **45**, 2513–2524 (2003).
69. Hussein, M. A. & Materials Abdul Samad Mohammed, and Naser Al-Aqeeli. Wear characteristics of metallic biomaterials: a review. 8, 5 : 2749–2768. (2015).

Acknowledgements
The authors would like to thank King Fahd University of Petroleum and Minerals for funding this study under Grant # ER221004.

Author contributions
M.A. Hussein: Conceptualization, Methodology, Investigation, Funding acquisition, project administration, writing – original draft, writing – review, and editing. A. Madhan Kumar: Investigation, Methodology, Data curation, writing – review, and editing. N.O. Ogunlakin: Investigation, Methodology, Data curation, writing – review, and editing. Nestor Ankah: Investigation, Data curation, writing- reviewing, and editing. M.A. Azeem: Investigation, Data curation, writing- review, and editing.All authors reviewed the manuscript.

Declarations

Competing interests
The authors declare no competing interests.

Additional information
Supplementary Information The online version contains supplementary material available at https://doi.org/10.1038/s41598-025-16657-3.

Correspondence and requests for materials should be addressed to M.A.H.

Reprints and permissions information is available at www.nature.com/reprints.

Publisher's note Springer Nature remains neutral with regard to jurisdictional claims in published maps and institutional affiliations.